Cellulose (2017) 24:519–533
DOI 10.1007/s10570-016-1179-4

ORIGINAL PAPER

Material properties of the cell walls in nanofibrillar cellulose foams from finite element modelling of tomography scans

Prashanth Srinivasa · Artem Kulachenko · Filip Karlberg

Received: 24 September 2016 / Accepted: 19 December 2016 / Published online: 26 December 2016

Abstract The mechanical properties of the nanofibrillar cellulose foam depend on the microstructure of the foam and on the constituent solid properties. The latter are hard to extract experimentally due to difficulties in performing the experiments on the micro-scale. The aim of this work is to provide methodology for doing it indirectly using extracted geometry of the microstructure. X-ray computed tomography scans are used to reconstruct the microstructure of a nanofibrillar cellulose foam sample. By varying the levels of thresholding, structure of differing porosities of the same foam structure are obtained and their macroscopic properties of the uniaxial compression are computed by finite element simulations. A power law relation, equivalent to classical foam scaling laws, are fit to the data obtained from simulation at different relative densities for the same structure. The relation thus obtained, is used to determine the cell wall material properties, viz. elastic modulus and yield strength, by extrapolating it to the experimental porosity and using the measured response at this porosity. The simulations also provide qualitative insights into the nature of irreversible deformations, not only corroborating the experimental results, but also providing possible explanation to the mechanisms responsible for crushable behaviour of the nanofibrillar cellulose foams in compression.

Keywords Nanofibrillar cellulose foam · Elastic modulus · Yield strength · X-ray tomography

P. Srinivasa · A. Kulachenko (✉) · F. Karlberg
Department of Solid Mechanics, School of Engineering Sciences, KTH Royal Institute of Technology, 10044 Stockholm, Sweden
e-mail: artem@kth.se

P. Srinivasa
e-mail: pns@kth.se

F. Karlberg
e-mail: filipkar@kth.se

Introduction

Nano fibrillar cellulose (NFC) foams are a class of low density cellular materials. These were pioneered by (Pääkkö et al. 2008) in their work on NFC aerogels. We have, in an earlier paper (Srinivasa et al. 2015) remarked on the distinction between NFC aerogels and NFC foams, and shall continue to reference it by the latter name. Since cellular materials play a preeminent role in many engineering applications, the development of a bio-degradable alternative to polymeric and inorganic cellular materials naturally becomes interesting and valuable. The mechanical properties of these materials have been the subject of many articles (Svagan et al. 2008; Sehaqui et al. 2010; Ali and Gibson 2013; Martoïa et al. 2016). Most of these works have concentrated on the role of chemical compositions in altering the microstructure, and thus to their effect on the macroscopic or bulk properties.

Some of these works have also alluded to the cell wall material properties of the foam under consideration, by using the classical foam scaling laws (Gibson et al. 1982; Gibson and Ashby 1982, 1988) to extrapolate to unit relative density (Sehaqui et al. 2010; Gordeyeva et al. 2016) or through micro indentation tests carried out on NFC thin films (Ali and Gibson 2013). To the best of our knowledge, these are the only two methods by which the cell wall material properties have been estimated for NFC foam materials until now.

The properties of the constituent solid material, also referred to as the cell wall properties, is of importance in evaluating the effect of the raw materials and the changes brought by various chemical treatments prior or during manufacturing. Isolating the solid material and carrying out physical experiments to determine the material properties is a formidable task owing to the length scales involved. Alternative methods include carrying out tests on structures made from material identical to those of the cell wall material. An example of which is the indentation tests carried out on NFC thin films (Ali and Gibson 2013). These are however not always representative of the actual material in the cell walls since what the cell walls experience during foam manufacturing differ to those in preparing NFC films. In this context, it is our aim to explore the possibility of estimating the cell wall material properties based on the direct finite element simulations on the structure that is reconstructed from tomography scans.

Reconstructed tomography scans of various cellular structures have been used before in simulations for varying purposes, ranging from studying the microstructural deformation mechanisms to inverse estimation of cell wall properties through parametric sweep (Maire et al. 2003; Caty et al. 2008; Jeon et al. 2009, 2010; Natesaiyer et al. 2015). One of the primary concerns in reconstructing cellular/porous structures from their tomography scans is the question of segmentation or thresholding. Usually, the value of the threshold required to get a clear microstructure does not necessarily correlate with the value required to match the porosity. Burdened with the same circumstance, we utilise the thresholding value as a parameter and reconstruct structures at differing levels of thresholding. We use the computed results from the series of simulations conducted on different porosity levels and the experimental results for the given porosity to arrive at the cell wall material properties using the scaling laws and extrapolation based on them.

Materials and methods

Material

There exist several methods to produce NFC foams, each having their own merits. For small scale production, the methods of freeze drying (Aulin et al. 2010b; Tchang Cervin et al. 2012), supercritical carbon dioxide (Sehaqui et al. 2011) drying are well suited, whereas when scaling up is desired Cervin et al. (2013) have demonstrated that cellulose foams with improved mechanical properties can be obtained by drying aqueous foams stabilised with surface-modified NFC. The primary focus of this work is to demonstrate a method to obtain cell wall properties from tomography simulations, and to use these simulations as a verification case for further large scale numerical simulations. Thus, we shall restrict ourselves to foams that were previously characterised experimentally. The foams used in this study were the same as those characterised experimentally in the study by Srinivasa et al. (2015) and the detailed description of the preparation procedure is found here.

The NFC foam used in this study was prepared at Innventia from anionic NFC obtained from carboxymethylation pre-treatment of the fibres (Pääkkö et al. 2007; Wågberg et al. 2008). After the carboxymethylation treatment, the fibres were treated with $NaHCO_3$ solution to increase the separation of fibres into nanofibrils. After being washed with deionized water and drained, the resulting dispersion was homogenised at 1700 bar using a high-pressure homogeniser. The NFC dispersion thus obtained was put in a mould and the mould was dipped into liquid nitrogen. Once frozen, the mould was vacuum ($<10^{-5}$ MPa) dried for 5 days. Two separate porosities, namely 98.96 and 98.13%, were obtained. These porosities were computed based on the percentage by weight of the cellulose in the CNF gel that was used to prepare the foams, which is a common method used with these materials (Chen et al. 2004; Diddens et al. 2008; Srinivasa et al. 2015). Since the porosity of the foams can be influenced by humidity, the porosities of the dry foams were also computed at two different conditions. Firstly, foam samples were dried at 110 °C

in an oven. They were then weighed on a chemical balance and their dimensions measured using digital calipers. At a relative humidity of 23% and temperature of 24.5 °C, the porosity of the two dried foams were calculated to be 98.99 ± 0.02 and $98.19 \pm 0.06\%$ respectively. The samples were then allowed to rest in a climate controlled chamber maintained at 40% relative humidity and temperature of 24.5 °C for 1 day, that is, the conditions the foams were scanned at. Subsequently, they were weighed and the porosities were calculated to be 98.85 ± 0.08 and $98.06 \pm 0.01\%$ respectively.

Methods

X-ray tomography

X-ray computed microtomography or X-ray tomography is a non-destructive method available to image the microstructure of porous and other materials. It relies on the usage of X-ray beams to scan a 3D object at various orientations, and obtaining a stack of images, also called "slices", that correspond to the 2D planes of the 3D object. These images are then used to reconstruct the spatial density distribution thereby providing the image of the 3D structure. The tomography scans in this work were carried out at the 4D-Imaging lab, Division of Solid Mechanics, Lund University. The instrument used was a Zeiss XRadia XRM 520 X-ray tomograph. The X-ray tube voltage was maintained at 80 kV and images of resolution 600 and 3039 nm were obtained. The tomography scans were obtained as a stack of grayscale images, which contain 16-bit unsigned data. The resolution in this case refers to the size of an individual voxel in 3-dimensions. Thus, each voxel is of dimension 600 nm $\times$ 600 nm $\times$ 600 nm. The tomography scans were carried out at a relative humidity of 40% at a temperature of 28 °C.

Image processing

The stack of images is processed as a whole and a series of image processing techniques are applied to reconstruct the foam structure from the scans. To begin with, a process called as histogram equalization is applied to the stack of images. This is done to alter the histogram of intensities into a desired shape. In general, the intensity values of the pixels/voxels in the image are mapped on such that the output has a more uniform distribution of intensities (Fisher et al. 2003). This has the effect of stretching the dynamic range and making details easier to see. It makes the histogram of the image to be better distributed, thereby providing better contrast.

This is followed by the thresholding, also called as binary segmentation, procedure. In this process, the grayscale image is converted into a binary image by setting all the voxels below a certain grayscale value to 0, and all voxels above this grayscale value to 1. It is this process that poses the biggest challenge and introduces ambiguities when reconstructing structures from tomography scans where there is considerable noise. The choice of the limits in thresholding is essentially the deciding factor between what we identify as material and what we identify as pore. It is clear that this also directly affects the porosity of the reconstructed structure. One of the suggested methods is to adjust the thresholding limit, such that the porosity of the obtained structure matches its original porosity. However, this is not always feasible for two important reasons. First, when reconstructing samples of small sizes, it is not necessary that the local porosity be identical to the original porosity of the material. Secondly, irrespective of the resolution of the scan, one is not certain if the cell walls are truly continuous/homogeneous or may themselves be porous (Fig. 1). In a study on the directional freezing of nanocellulose dispersions and their effect on the network like structures in cell walls of the hydrogels so formed, (Munier et al. 2016) have suggested that there exists an inverse relationship between the density of the cell walls and the degree of fibrillar orientation in the same cell walls. This suggests that in structures formed by frozen templates, like the foams in our study, the cell wall density is an important parameter that might affect the mechanical properties. The inverse relationship between resolution and the sample size also proves to be the limiting factor. In our case, we focus on the deformation mechanisms at the cellular level. Hence, we limit ourselves to high resolution, but small sample size. It is to be noted that despite the choice of higher resolution, the pores in the cell walls cannot always be resolved.

After the thresholding process, there remain isolated or unconnected voxels which have been assigned as material. This happens because of lack of a sharp

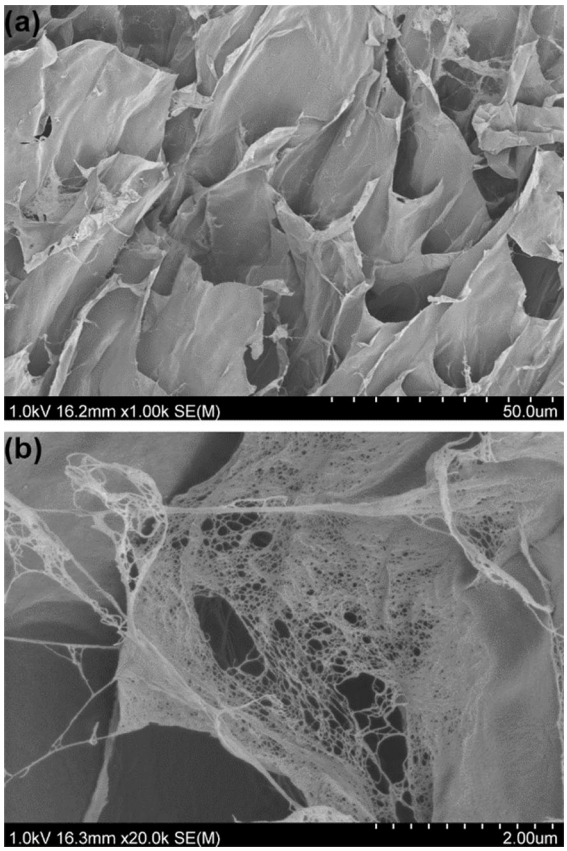

Fig. 1 SEM image of the current foam sample (98.96% porosity) demonstrating that the cell walls which appear continuous at higher resolution might actually be porous

contrast between material and void/pore even after histogram equalisation. These voxels have intensity values that correspond to the material, but are not connected to the main structure. This is taken to be an artefact, and removed using an "island removal" algorithm available in Avizo. This algorithm searches for voxel clusters that do not have any connectivity to a neighbouring pixel or voxel. Since this algorithm is controlled by the minimum size of the isolated voxel assemblies, not all the isolated voxels are removed. The effect of histogram equalization, thresholding and island removal is shown in Fig. 2. Finally, the three-dimensional surface is reconstructed by a triangulated approximation of the material surface. It is seen that this process does not always provide us with a continuous structure, which is necessary for finite element simulation. Therefore, additional pre-processing steps are required as described below.

Meshing

The triangulated surface obtained earlier needs to be rid of the loose unconnected structures. This is done in Matlab and is subject to the assumption that at least one vertex of the largest contiguous structure lies at the top or bottom surface of the cylindrical foam sample. This triangulated surface geometry is then meshed using Altair Hypermesh with tetrahedral elements having the maximum allowed element edge size of 2.5 microns. The meshing is done with tetra elements that are compatible with Ansys/LS-Dyna pre-processing module where another round of shape checking of the elements is carried out. The second round of shape checking for the elements is done to eliminate those elements, which do not meet the default mesh quality criteria such as tetra collapse ratio. This has the effect of further reducing the material from the considered sample, but it is seen that its effect on porosity is negligible and is limited to altering the porosity calculations only to the second or third decimal place. The final porosity of the thresholded and subsequently meshed structure is computed based on the total volume of the elements in the mesh divided by the volume of the cylinder that encloses the sample. Finally, the uni-axial compression simulations are carried out in LS-Dyna using implicit quasi-static computation. The advantage of using LS-Dyna for this type of simulation resides in the ability to detect surface–surface contact automatically in a robust fashion.

Erosion

Successive thresholding operation at different levels has the effect of diminishing the material in the reconstructed structure. This does not happen in a uniform manner, and the method runs the risk of losing structural details as the thresholding value is increased. Thus, an alternative to the method described in the previous section is to threshold the structure at the lowest possible value to retain the maximum portion of the geometry. Later, the clean-up, reconstruction and meshing of the structure is carried out. This structure is then digitally scanned into two-dimensional slices, represented as binary images. Following which, two morphological operations viz., dilation and erosion are carried out. These operations together are called as morphological

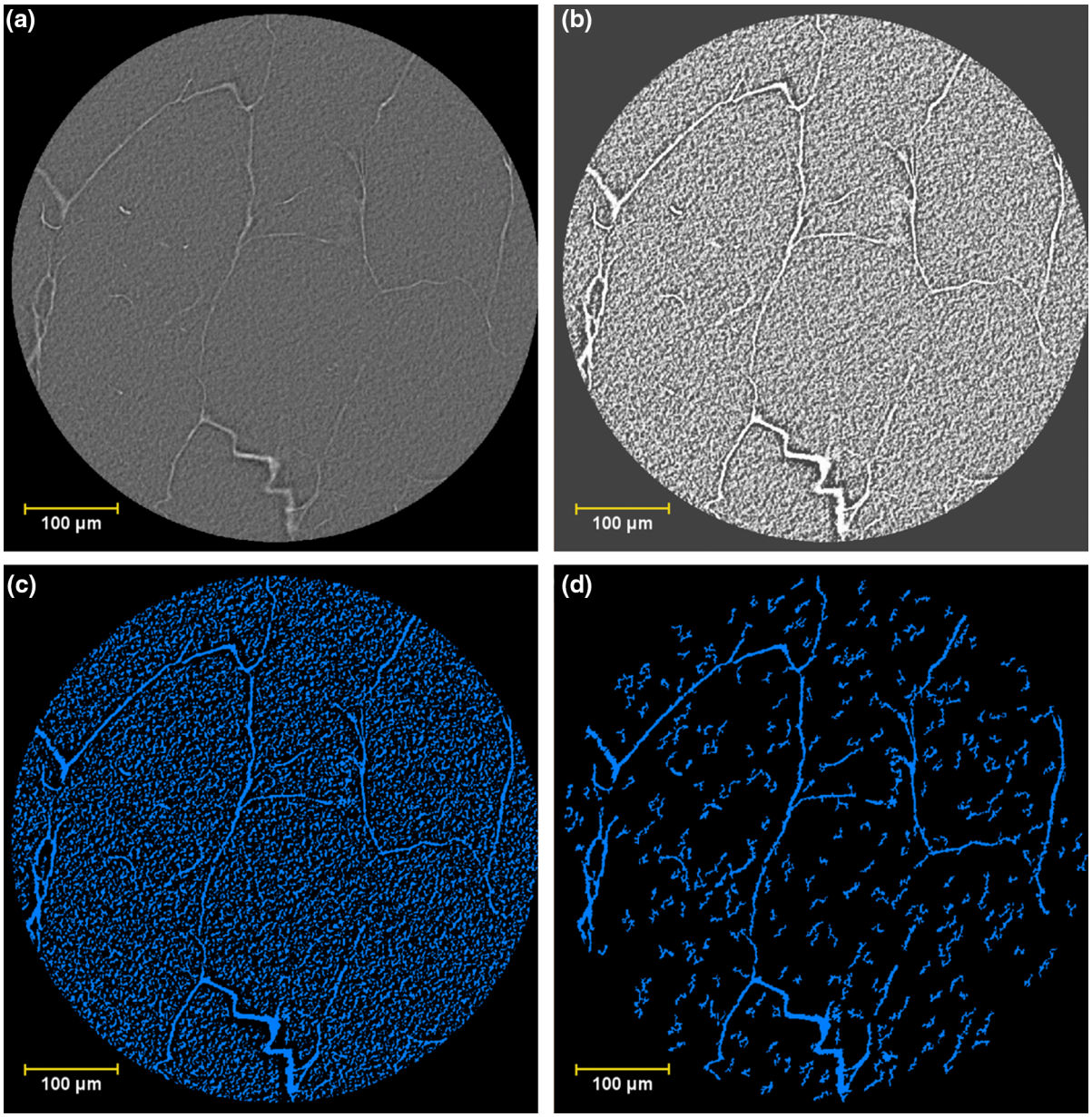

Fig. 2 The effect of **b** histogram equalization, **c** thresholding and **d** island removal on a typical 2D slice of tomography scan (**a**)

closing and are used to retain regions which have shapes identical to the structural element used in these operations (Fisher et al. 2003). The scanned structure typically has some pores in the cell walls. The dilation operation has the effect of growing the pixels in the foreground while rendering the holes smaller and smaller (Fisher et al. 2003). After a sufficient level of dilation is carried out, the erosion operation which has the effect of thinning the foreground structure is applied (Fisher et al. 2003). The effect of these operations and the reconstructed surfaces are shown in Figs. 3 and 4.

The porosity of the final structure is computed based on the sum of the element volume and the volume of the cylinder that encompasses the scanned structure. The porosities obtained from structures which are thresholded vary from 96.02% at the lowest level of thresholding to 98.41% at the highest level.

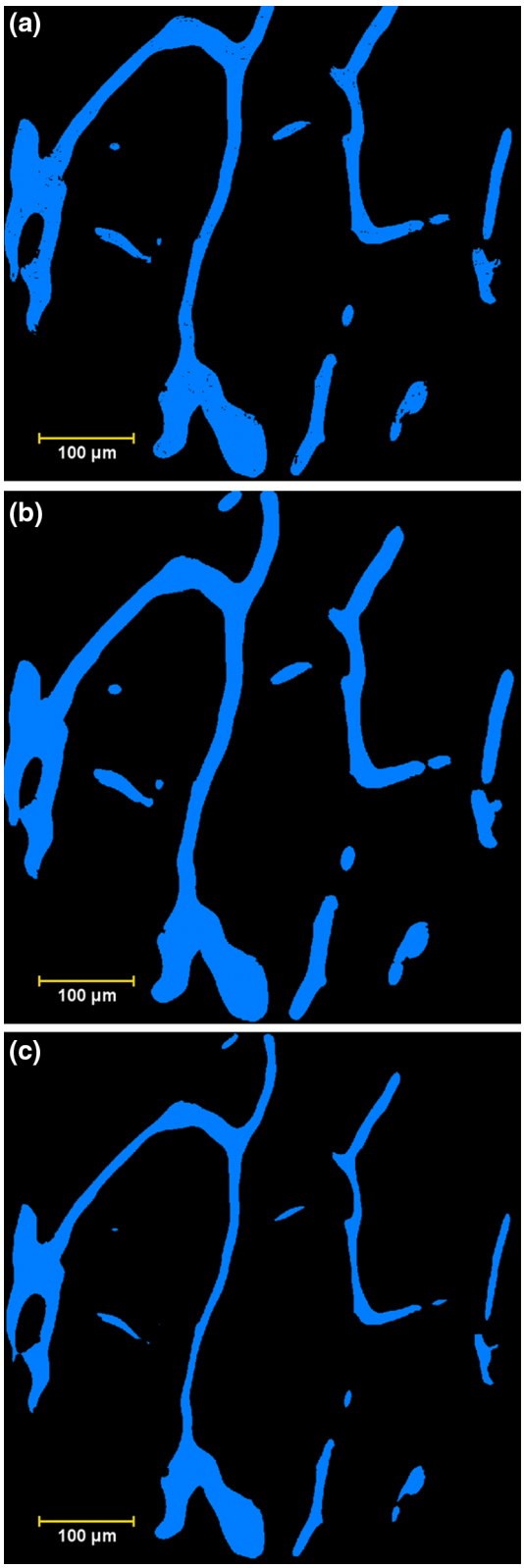

◀**Fig. 3** Morphological operations of **b** dilation and **c** erosion on a typical digitally scanned 2D slice (**a**) (binary image). Observe the thinning of the cell walls in (**c**)

The porosities of the structures obtained by the process of erosion vary between 92.32 and 96.89%. It is to be noted that the foam that is used in this study has a measured porosity of 98.96%, which means we were unable to attain this porosity level from the tomography data.

Pore volume measurements

The calculation of the cell wall density requires the volume of the micro- and meso-pores to be estimated. This was done by nitrogen gas desorption using ASAP 2020 (Micromeritics Instrument Corporation, Norcross, GA, U.S.A) equipment at Innventia AB. The measurements were based on the method of Barrett-Joyner-Halenda (BJH) and the pore volumes were estimated from the N_2 desorption curve at 77 K. The pore volume thus obtained was used to calculate the porosity of the walls through the method and equations outlined in (Gordeyeva et al. 2016). The wall density (ρ_{wall}) is given by Eq. 1.

$$\frac{1}{\rho_{\text{wall}}} = \frac{V_{\text{pore}}}{m} + \frac{1}{\rho_{\text{sk}}} \tag{1}$$

Here, V_{pore} corresponds to the micro- and meso-pore volume obtained from N_2 desorption and ρ_{sk} is the skeletal density, which here corresponds to the CNF density of 1500 kg/m^3. Subsequently, the porosity of the cell wall is calculated based on Eq. 2.

$$\varphi_{\text{wall}} = \left(1 - \frac{\rho_{\text{wall}}}{\rho_{\text{sk}}}\right) \tag{2}$$

Finite element model

Boundary conditions

The choice of the boundary condition was motivated from the experimental conditions and results that were reported in our earlier work (Srinivasa et al. 2015), which we will be using as a reference for extrapolation based on the scaling laws. In the case of uni-axial

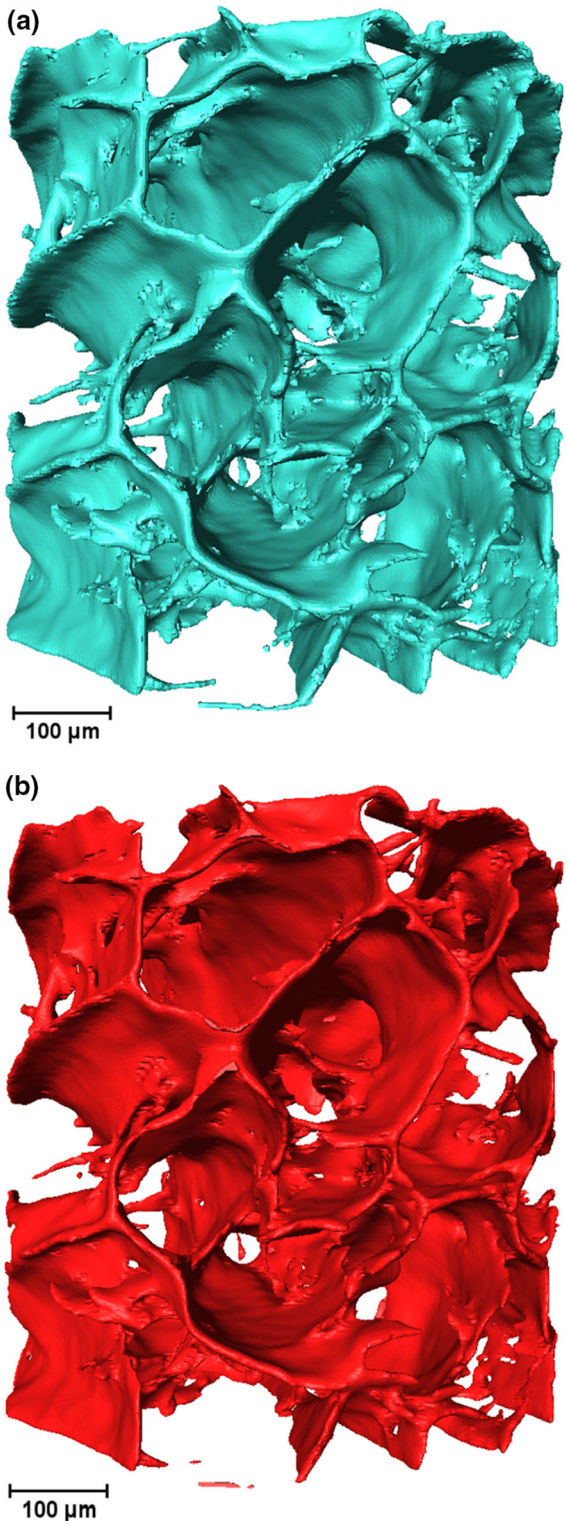

◀**Fig. 4** Reconstructed surface, not yet meshed, **a** before and **b** after the morphological operations of dilation and erosion. Notice the thinned cell walls before and after morphological closing

compression, one of the plates remained clamped/-fixed, while the other was used to load and unload the sample. This condition was retained in the simulations where two square plates made of steel were modelled. The bottom plate was fixed while the top plate compressed the cylindrical foam sample. Surface to surface contact is defined between the plate and foam surfaces, along with a general contact of all surfaces within the foam itself. We assume frictionless contact between the plates and foam. The outer surface of the cylindrical sample is not constrained in the lateral directions. Usually, this requires a large enough sample volume to avoid any boundary effects. Alternatively, periodic boundary conditions, which are known to produce stiffer response (Miehe and Koch 2002; Mesarovic and Padbidri 2005), need to be applied. The cylindrical sample, since it does not tile the three-dimensional space, precludes the usage of periodic boundary conditions, unless modifications such as embedding into equivalent continua as presented in (Natesaiyer et al. 2015) are made. With the trade-off between resolution and sample size limiting the size of the sample, we are compelled to use unconstrained boundary conditions on the lateral surfaces. Displacement boundary conditions are applied on the steel plates and contact is defined between the foam sample and the steel plates, while also accounting for contact within the foam surfaces.

Material properties

One of the aims of this work is to retrieve the material properties of the cell wall, by studying the scaling of the properties with respect to its thresholding. However, it is necessary to start with a reasonable estimate of the properties. We utilise an elasto-plastic material model with isotropic hardening and do not consider any strain rate effects. This model is characterised by the Young's modulus, yield stress and the tangent modulus. Various estimates of the Young's modulus are available, all of which have been measured

indirectly through scaling laws (between 1 and 10 GPa) (Sehaqui et al. 2010), or even through hardness indentation tests on NFC thin films (Ali and Gibson 2013). The estimate from indentation tests may not be very accurate since: (1) the thin films may not be representative of the cell walls, (2) manufacturing thin films introduce directionality and fibril orientation is not isotropic. The yield stress has also been estimated by similar scaling laws to be between 67 and 227 MPa (Ali and Gibson 2013). There can be directionality to the fibre network that comprise the cell walls, based on the method of preparation (Munier et al. 2016). This is likely to render the cell walls transversely isotropic. However, we posit that for bending dominated deformations, the out of plane properties will not affect the results unless the transverse shear stiffness is low. The measurements of cell wall density indicate that the cell walls are sufficiently dense, justifying the use of isotropic material for describing the cell wall constitutive response for this type of deformation. At the outset, we begin our simulations assuming the material properties to be as mentioned in Table 1.

Choice of the finite element

In problems involving meshing 3D geometries reconstructed from scans, the choice of the finite element could be considered to be dependent on two important criteria. First, the accuracy of representation of the reconstructed structure and secondly, the cost and feasibility of computation. In our case, for the lowest threshold, about 7 million elements are necessary to represent the geometry accurately. Introducing quadratic interpolation with mid nodes to the tetra elements makes the computational cost prohibitive along with introducing convergence problems related to increased sensitivity to mesh distortion. Thus, we resort to constant stress 4-node tetrahedral element. This is however known to lead to a stiffer than actual response, particularly in bending dominated problems as the one we face in this work. It is however possible to get a reasonable estimate of this error, by considering a problem which is bending dominated with comparable geometrical dimensions and identical material parameters as that of the foam.

Convergence check and element benchmark

In order to check the validity of the tetrahedral element used in the meshing of foam structure, we consider a three-dimensional hexagonal honeycomb structure of similar cellular dimensions in terms of cell size and wall thickness. We consider a structure with 50 cells, where each of the hexagonal cells have a nominal size of 150 microns, and the cell walls are 10 microns thick. We consider three different elements: 4-node tetrahedral element without mid nodes, 10-node tetrahedral element with mid-nodes and a 4-node shell element. The tetra element has three translational degrees of freedom at each nodal point, uses a linear interpolation function for displacements yielding constant stress within the element. The 10-node tetrahedral element also has three translational degrees of freedom at each nodal point but is characterised by higher order interpolation functions resulting in linear variation of the stresses along its edges. The 4-node shell element has three translational and three rotational degrees of freedom at each node, and uses five integration points through the thickness.

We consider an elasto-plastic material model with properties identical to those used for foam and as given in Table 1. We restrict ourselves to strain levels of 10% which is enough to demonstrate the difference in the stiffness and yield stress between solutions with different elements. The non-linear solution procedure uses an implicit time integration scheme. The results from the analysis is presented in Fig. 5.

We begin with a coarse discretization of the structure, utilising one element per thickness. It is observed that this resolution is sufficient for both the tetrahedral element with mid-nodes and the shell element. Using two elements per thickness does not alter the solution appreciably for these two element types. The tetrahedral element without mid nodes is

Table 1 Material properties used for initial simulations

Young's modulus E (GPa)	Poisson's ratio ν (–)	Yield stress σ_Y (MPa)	Tangent modulus σ_T (MPa)
20	0.3	100	4000

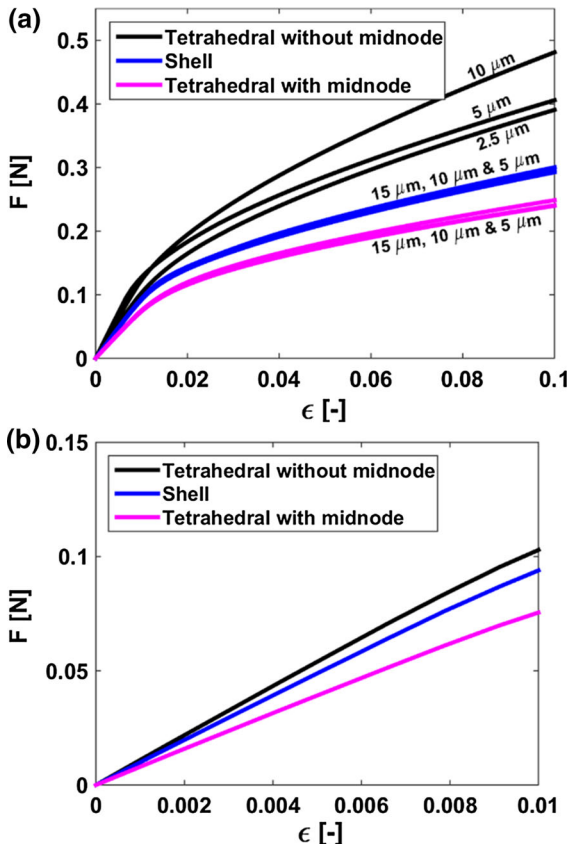

Fig. 5 Element convergence check on the 3D hexagonal honeycomb structure. Image **b** zooms in on the initial slope of the curves in (**a**)

however characterised by a softening solution even at 2.5-micron size, which amounts to a resolution of 4 elements in the thickness direction. In the non-linear region, the tetrahedral solution differs from the shell solution (in an average relative error sense) by approximately 23%, and from the tetrahedral mid-node solution by approximately 37%. In the linear elastic region, these errors reduce to approximately 11 and 29% respectively. A stiffer response of the shell-based model is explained by overlapping mass in the connecting corners of the honeycomb foam. The resolution of the geometric features in the tomography scan requires a very fine mesh. The usage of tetrahedral elements without mid nodes is motivated by this requirement. Although the mid-node element provides convergence at one-fourth the mesh size, the mesh size requirement in our study is governed by the need to have a fine enough mesh so as to capture the geometric features while also providing better convergence by avoiding severe element distortions to which the mid node elements are susceptible to.

Without resorting to comparisons with experiments, it is not possible to ascertain which of the shell and tetrahedral mid-node solutions are acceptable. However, having characterised to an extent the deviation within these element types, using tetrahedral element with mid nodes or the shell element is precluded for the following two important reasons: (1) for the actual structure reconstructed from tomography scans, it is not possible to extract its mid surface, which is a requirement in order to mesh with shell elements; (2) introducing mid node tetrahedral elements into the mesh makes the computational cost prohibitively expensive. The usage of tetrahedral elements and its associated stiff response has important bearing on the results and they are discussed in the respective section.

Results

Effect of thresholding on the compressive stress–strain response

The full compressive stress–strain response parameterised against thresholding (and thus against porosity) is presented in Fig. 6. The results from varying the porosity of the structure using erosion is presented in Fig. 7. The response is qualitatively along the expected lines (Fig. 8), with an initial linear elastic region, followed by constantly increasing stress (identified with the stress plateau in some cases), and an accelerated increase in the stress levels at strains beyond 50%. The unloading curve also qualitatively agrees with those from experiments (Srinivasa et al. 2015), exhibiting large irreversible deformations upon unloading. The peak stress levels attained at the end of densification is seen to reduce with increasing thresholding values.

Generally, the densification stress is attributed to contact of the cell walls. It is of interest to note that for the geometry that remains largely unchanged, except for reduction in thickness of the cell walls, the peak densification stress is not dependent on contact alone. The results from erosion are consistent with those from regular thresholding and reconstruction, except for the fact that it is not possible to reach lower levels of porosity unlike in the latter method.

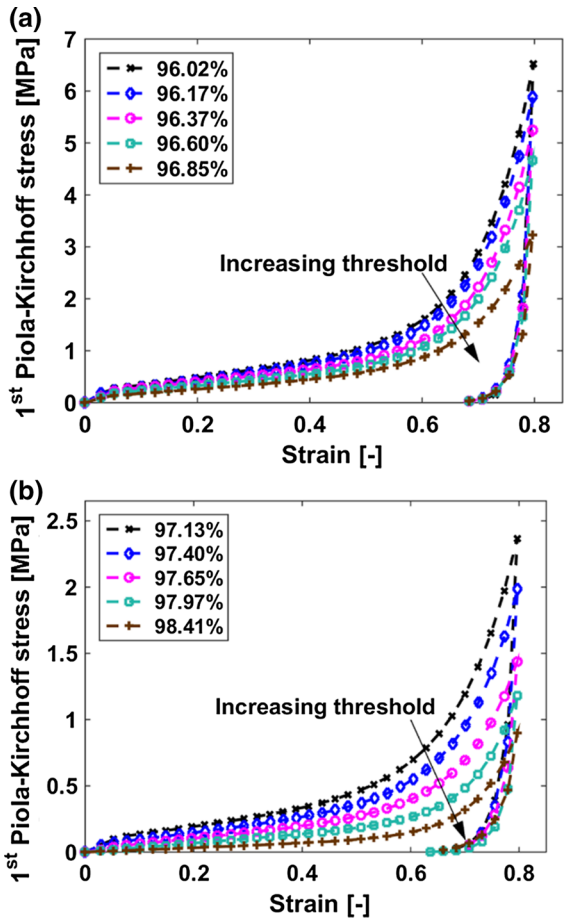

Fig. 6 Compressive stress–strain curves for different levels of thresholding which result in structures of different porosities

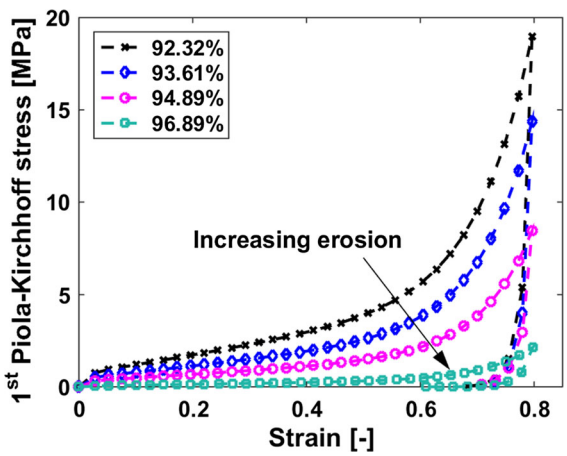

Fig. 7 Compression stress–strain curves for structures obtained through the method of erosion

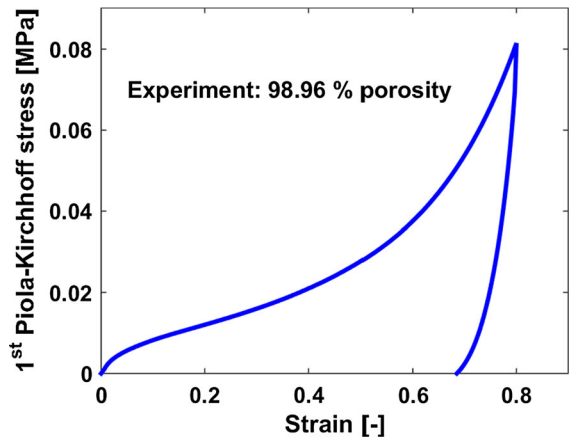

Fig. 8 Typical experimental compressive stress–strain curve for NFC foam

Mechanisms of microstructural deformation

In the recently published work (Martoïa et al. 2016), in situ tomography measurements were made during a compression experiment and these scans were used to explore the mechanisms responsible for strain hardening like behaviour in the response of NFC foams. We are interested to see if these effects can be seen in the direct finite element simulations of the tomography scans. The compressive response of the structure with 96.17% porosity is shown in Fig. 9. The points marked "A" to "F" correspond to the snapshots from simulations at different strain levels presented in Fig. 10. A typical cell (second column in Fig. 10) and two of its

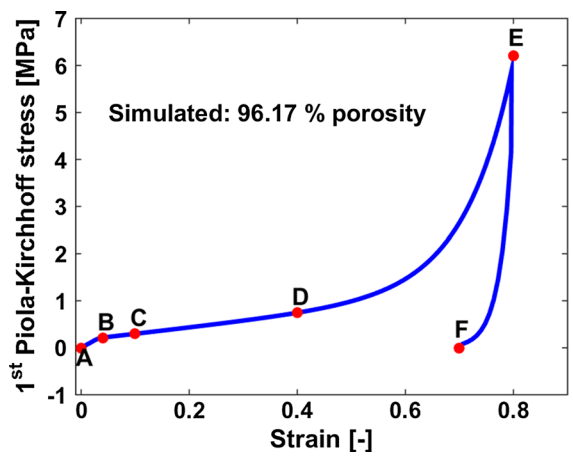

Fig. 9 Compressive stress–strain response from the simulation of 96.17% porosity structure

edges (third column in Fig. 10) are isolated from the full structure and contours of the values of the equivalent von Mises stresses are shown at different strain levels.

The purported linear elastic region extends to a strain level of 0.04 (point B). At around this point, there is already some small regions of plastic deformation that begin to appear in the cell walls. These regions serve as sites for the formation of plastic hinges or bands, about which the collapse of the cell wall happens. At strain levels of 0.1 (point C), this hinge/band formation is almost complete. These hinges/bands interestingly seem to appear along the vertices of the cell as evidenced in the two vertices of the same cell isolated in the third column of Fig. 10. Between the strain levels of 0.1 (point C) and 0.4 (point D), there is some strain hardening as the cell walls continue to collapse. At peak strain level of 0.8 (point E), the collapse is complete and the vertices are almost flattened out. In the course of this transformation, the curvature of the cell walls has changed, producing geometric contribution in addition to strain hardening in the so-called plateau region. Upon unloading, at strain levels where the macroscopic stress has reduced to 0, the microstructure displays almost complete permanent plastic deformation. Only minor regions regain their deformation, and possibly some surfaces (as is evidenced in the surface of the vertex).

Varying of elastic modulus and scaling in the elastic region

The elastic modulus (E_s) was varied between 10 GPa and 30 GPa in steps of 5 GPa. This is done for every thresholded structure. The elastic modulus of the thresholded structure (E^*) is obtained from the slope of the macroscopic stress–strain curve. Subsequently, the scaling law for the elastic region (Eq. 3) (Gibson and Ashby 1988) is used to estimate the constants C_1 and n_1 for every assumed value of E_s.

$$\frac{E^*}{E_s} = C_1 \left(\frac{\rho^*}{\rho_s}\right)^{n_1} \tag{3}$$

A plot of the relative densities against the ratio of macroscopic modulus to cell wall modulus $\left(\frac{E^*}{E_s}\right)$ is presented in Fig. 11. The estimated values of the cell wall modulus are computed by extrapolating the line of scaling to include the porosity of the actual scanned sample. The results from the highest porosity (98.41%) was neglected since the stress–strain response is not reliable owing to insufficient elements through the thickness of extremely thin walls.

Varying of the yield stress and scaling of the plateau stress

The yield stress (σ_y) of the cell wall material is varied between 50 and 90 MPa in steps of 10 MPa. A procedure identical to the varying of elastic modulus is adopted and the plateau stress (σ_p) is calculated from the macroscopic stress–strain curve. The definitions of the plateau stress vary, and is variously defined as the stress at initiation of plastic collapse to the average of the stress values in the actual plateaus region of the stress–strain response. Since the compressive response of the NFC foam shows gradual increment of the stress even in the so-called plateau region, we adopt the following definition. The plateaus stress is taken to be the stress value at which the slope of the stress–strain curve deviates from that of the initial linear region by more than 5%. Subsequently, the scaling law for the plateau stress (Eq. 4) (Gibson and Ashby 1988) is used to estimate the constants C_2 and n_2 for every assumed value of σ_y.

$$\frac{\sigma_p}{\sigma_y} = C_2 \left(\frac{\rho^*}{\rho_s}\right)^{n_2} \tag{4}$$

A plot of the relative densities against the ratio of plateau stress to cell wall yield stress $\left(\frac{\sigma_p}{\sigma_y}\right)$ is presented in Fig. 12. The values obtained from the structure with porosity of 97.97% was neglected because it showed unusual deviation from the rest of the data, and was considered an outlier. The reason of the outlying is presumably an insufficient number of integration points required to resolve the plastic behaviour through the thickness of the cell wall.

Discussion

The Eqs. 3 and 4 have the form of scaling laws for open cells as derived from the idealisation of an unit cell in a lattice structure (Gibson and Ashby 1982, 1988; Ashby 2006). For the case of bending dominated deformation in open cell structures, the

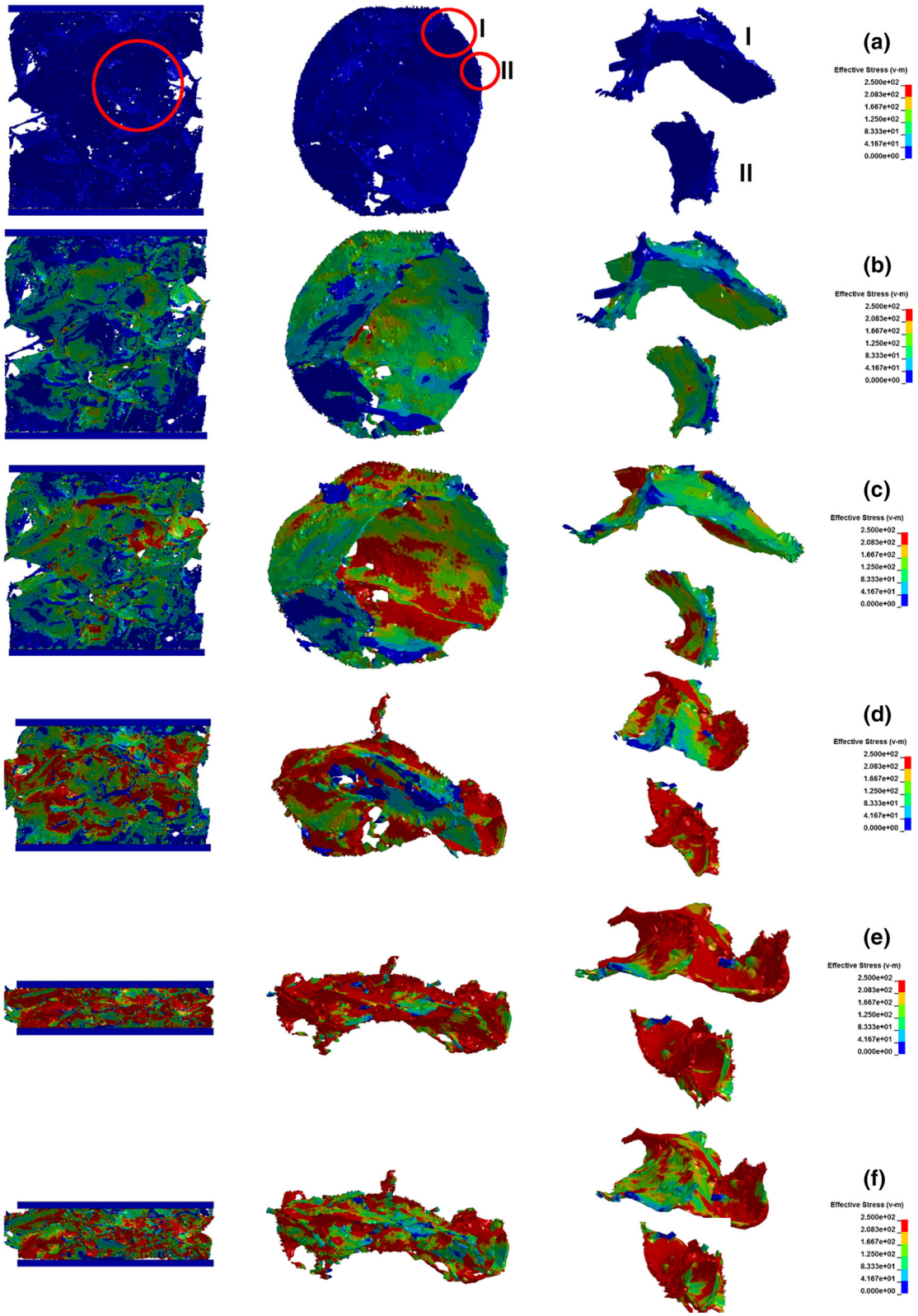
I
II
I
II
(a)
Effective Stress (v-m)
2.500e+02
2.083e+02
1.667e+02
1.250e+02
8.333e+01
4.167e+01
0.000e+00
(b)
Effective Stress (v-m)
2.500e+02
2.083e+02
1.667e+02
1.250e+02
8.333e+01
4.167e+01
0.000e+00
(c)
Effective Stress (v-m)
2.500e+02
2.083e+02
1.667e+02
1.250e+02
8.333e+01
4.167e+01
0.000e+00
(d)
Effective Stress (v-m)
2.500e+02
2.083e+02
1.667e+02
1.250e+02
8.333e+01
4.167e+01
0.000e+00
(e)
Effective Stress (v-m)
2.500e+02
2.083e+02
1.667e+02
1.250e+02
8.333e+01
4.167e+01
0.000e+00
(f)
Effective Stress (v-m)
2.500e+02
2.083e+02
1.667e+02
1.250e+02
8.333e+01
4.167e+01
0.000e+00

◀**Fig. 10** Snapshots of the simulation at different stages of compression. The porosity of the foam sample shown in figure is 96.17%. The *red circular marking* on the figure in the *top left* corresponds to a typical cell and is shown for tracking purpose. This cell is isolated and the localised deformation as it undergoes compression is shown in the *second column*. The *third column* corresponds to the two edges of the cell (marked *I* and *II*) and their localised deformation at various macroscopic strains. (Color figure online)

constant of proportionality C_1 is expected to be unity, while C_2 has been previously shown to be approximately 0.3 (Gibson and Ashby 1982, 1988; Ashby 2006). Since the mechanisms in yielding of a fully dense constituent solid is dissimilar to that in the

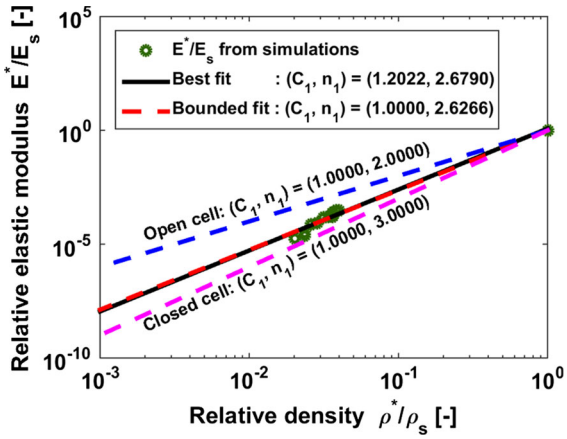

Fig. 11 Scaling of the ratio of macroscopic elastic modulus to the assumed cell wall elastic modulus

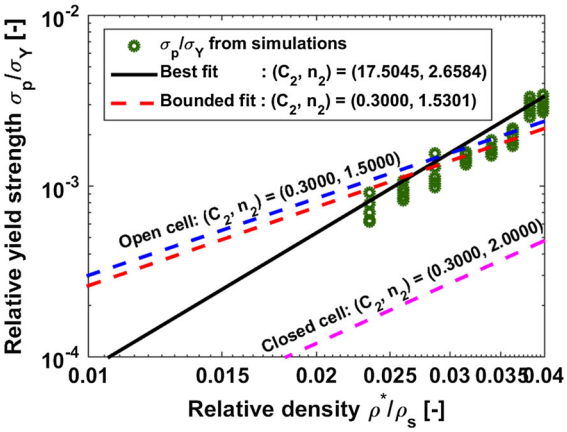

Fig. 12 Scaling of the ratio of macroscopic plateau stress to the assumed cell wall yield stress

porous structure, it is to be anticipated that constant C_2 is not unity. The exponents n_1 and n_2 in bending dominated problems are analytically derived (Gibson and Ashby 1982, 1988) to be 2 and 3/2 respectively. When many structures of different porosities are considered, these constants shed light on the deformation mechanisms at play in the microstructure. In the present case, it is important to note that we have a structure which essentially remains the same, while the differing levels of thresholding remove material from the structure in a non-uniform manner thereby altering its porosity. The best fit is obtained with $C_1 = 1.2022$ and $n_1 = 2.679$, showing a stronger than expected dependence on relative density. The microstructure considered here is indeed quite different from an idealised open cell structure. It is not dominated by strut like cellular structures nor is the material concentrated on the edges while retaining thin faces. For an ideal closed cell structure, the value of the exponent is expected to be 3. It is clear from the tomography scans as well as the variation of the relative elastic modulus with relative density Fig. 11 that this structure lies somewhere in between an open and closed cell structure. The exponent $n_1 = 2.679$ suggests that the linear elastic deformation is dominated by the bending of plate like cell wall structures.

Usually, the value for the cell wall elastic modulus is obtained from extrapolating the scaling laws to a fully dense material where $\frac{\rho^*}{\rho_s}$ is unity. Since we confine ourselves in this work to a single structure, and our differing porosities are obtained by varying the threshold levels, we extrapolate towards the actual porosity of the structure. Since the value of the macroscopic elastic modulus for the foam is known, we compute the cell wall modulus based on Eq. 5.

$$E_s = \frac{E^*_{exp}}{\overline{C_1}\left(\frac{\rho^*}{\rho_s}\right)^{\overline{n_1}}} \tag{5}$$

where $\overline{C_1}$ and $\overline{n_1}$ are the average values of the constants obtained through simulations at different thresholds. Our estimate for the Young's modulus based on the above method is 29.78 GPa. This is significantly higher than values of 1.2 GPa estimated by Sehaqui et al. (2010), 8.65 GPa reported by Ali et al. (2013) and 3.9–5.7 GPa by Gordeyeva et al. (2016). The foams in the study by Sehaqui et al. were reported to have open cell polyhedral structure while

the value for the cell wall modulus in Ali et al. (2010a) came from an indentation test on NFC thin films. It is interesting to note that our value for the Young's modulus compares to the highest value of elastic modulus reported for cellulose nanopaper (Kulachenko et al. 2012).

The value for the yield stress of the cell wall material computed by method similar to the elastic modulus, i.e. by extrapolating to the actual porosity value, and gives a value of 40.76 MPa. This again contrasts with the values of 67 and 227 MPa reported by Sehaqui et al. and Ali et al. respectively. The obtained value for the constant C_2 in case of the best fit is very high as compared to the previously reported values (much less than unity) for this constant. While this indeed raises some concerns, it must be noted that the choice of the scaling law is only incidental and any function that captured the variation of the two related properties (relative density and relative yield strength) would have sufficed and not raised concerns regarding the physicality. The exponent of the scaling law is higher than the anticipated value for closed cells ($n_2 = 2$) undergoing plastic collapse. This is usually attributed to a disordered microstructure but there could also be the possibility of a competing mechanism, namely elastic collapse or buckling, for which the exponent is expected to be ($n_2 = 3$) for closed cells. While the deformation mechanism observed in a typical cell (Fig. 10) suggests plastic collapse, some of the isolated or connecting sheet like structures could buckle contributing to this high value of the exponent.

The accuracy of this estimation is greatly affected by the accuracy of the porosity measurements in the experiment. The value of porosity considered in the calculation assumes that the volume is preserved between the wet and dry states and neglects the effects of humidity. If the effect of humidity on the porosity is accounted for (98.85% instead of 98.96%), then the estimate of the elastic modulus drops to 22.75 GPa and that of the yield stress to 31.12 MPa. From the N_2 desorption test, the pore volume in the cell walls was found to be 0.03850 cm^3/g. Thus, porosity of the cell walls, based on Eqs. 1 and 2, was estimated to be 5.45%. This suggests that the value of the modulus might be influenced by the thresholding procedure, particularly at low thresholding values as this leads to fully dense cell walls. In addition, the accuracy is affected by the choice of the boundary conditions (additional constraints will produce stiffer response and thus decrease the predicted modulus), element type (having softer response in the simulation will decrease the modulus). Finally, the considered size may not be representative for the selected structures. The impact of these potential problems is yet to be explored.

Conclusions

This study used the tomography scan of a nanofibrillar cellulose foam at high resolution to construct a finite element model, and evaluate the cell wall material properties. Since the local porosity of the structure need not be identical to the actual foam porosity, we threshold the scans at different levels to obtain structures of differing porosities. These structures are then simulated for uniaxial compression, with differing values for the cell wall elastic modulus and yield strength. These simulations provide a way of calculating the cell wall properties, knowing the equivalent macroscopic properties from experiments. The estimate of Young's modulus is given to be 29.78 GPa, which turns out to be quite high as compared to the previously estimated values. The value of the yield strength is found to be 40.76 MPa. In the simulations, we also observe evidence for plastic collapse through plastic hinge formation in the cell walls, thereby corroborating experimental observations reported elsewhere (Martoïa et al. 2016).

Under any circumstance, the geometrical reconstruction and the values obtained through the method described in this article can serve as a verification case for the artificial reconstruction algorithms for such foams. By reconstructing the sizes considered in this work, verifying the obtained compressive response, we can create larger structures and evaluate thoroughly the effect of size and boundary conditions.

Acknowledgments The authors wish to acknowledge BiMac Innovation for the financial support. We wish to thank Stephen Hall at the division of Solid Mechanics, Lund University for his assistance with the tomography scans. We wish to thank Åsa Blademo and Jiebing Li at Innventia AB for assistance with the nitrogen desorption measurements, and Irene Linares Arregui at the Solid Mechanics laboratory for help with porosity measurements. The authors also wish to thank Prof. Lars Wågberg from the Fiber and Polymer Technology department for his valuable comments.

References

Ali ZM, Gibson LJ (2013) The structure and mechanics of nanofibrillar cellulose foams. Soft Matter 9:1580. doi:10.1039/c2sm27197d

Ashby MF (2006) The properties of foams and lattices. Philos Trans A Math Phys Eng Sci 364:15–30. doi:10.1098/rsta.2005.1678

Aulin C, Gällstedt M, Lindström T (2010a) Oxygen and oil barrier properties of microfibrillated cellulose films and coatings. Cellulose 17:559–574. doi:10.1007/s10570-009-9393-y

Aulin C, Netrval J, Wågberg L, Lindström T (2010b) Aerogels from nanofibrillated cellulose with tunable oleophobicity. Soft Matter 6:3298. doi:10.1039/c001939a

Caty O, Maire E, Youssef S, Bouchet R (2008) Modeling the properties of closed-cell cellular materials from tomography images using finite shell elements. Acta Mater 56:5524–5534. doi:10.1016/j.actamat.2008.07.023

Cervin NT, Andersson L, Boon Sing Ng J et al (2013) Lightweight and strong cellulose materials made from aqueous foams stabilized by nanofibrillated cellulose. Biomacromolecules 14:503–511

Chen W, Lickfield GC, Yang CQ (2004) Molecular modeling of cellulose in amorphous state part II: effects of rigid and flexible crosslinks on cellulose. Polym (Guildf) 45:7357–7365. doi:10.1016/j.polymer.2004.08.023

Diddens I, Murphy B, Krisch M, Muller M (2008) Anisotropic elastic properties of cellulose measured using inelastic X-ray scattering. Macromolecules 41:9755–9759

Fisher R, Perkins S, Walker A, Wolfart E (2003) HIPR. In: Hypermedia image process. http://homepages.inf.ed.ac.uk/rbf/HIPR2/hipr_top.htm

Gibson LJ, Ashby MF (1982) The mechanics of three-dimensional cellular materials. Proc R Soc A Math Phys Eng Sci 382:43–59. doi:10.1098/rspa.1982.0088

Gibson LJ, Ashby MF (1988) Cellular solids. Pergamon Press, New York

Gibson LJ, Ashby MF, Schajer GS, Robertson CI (1982) The mechanics of two-dimensional cellular materials. Proc R Soc Lond A 382:25–42. doi:10.1098/rspa.1983.0054

Gordeyeva KS, Fall AB, Hall S et al (2016) Stabilizing nanocellulose-nonionic surfactant composite foams by delayed Ca-induced gelation. J Colloid Interface Sci 472:44–51. doi:10.1016/j.jcis.2016.03.031

Jeon I, Katou K, Sonoda T et al (2009) Cell wall mechanical properties of closed-cell Al foam. Mech Mater 41:60–73. doi:10.1016/j.mechmat.2008.08.002

Jeon I, Asahina T, Kang KJ et al (2010) Finite element simulation of the plastic collapse of closed-cell aluminum foams with X-ray computed tomography. Mech Mater 42:227–236. doi:10.1016/j.mechmat.2010.01.003

Kulachenko A, Denoyelle T, Galland S, Lindström SB (2012) Elastic properties of cellulose nanopaper. Cellulose 19:793–807. doi:10.1007/s10570-012-9685-5

Maire E, Fazekas A, Salvo L et al (2003) X-ray tomography applied to the characterization of cellular materials. Related finite element modeling problems. Compos Sci Technol 63:2431–2443. doi:10.1016/S0266-3538(03)00276-8

Martoïa F, Cochereau T, Dumont PJJ et al (2016) Cellulose nanofibril foams: links between ice-templating conditions, microstructures and mechanical properties. Mater Des 104:376–391. doi:10.1016/j.matdes.2016.04.088

Mesarovic SD, Padbidri J (2005) Minimal kinematic boundary conditions for simulations of disordered microstructures. Philos Mag 85:65–78. doi:10.1080/14786430412331313321

Miehe C, Koch A (2002) Computational micro-to-macro transitions of discretized microstructures undergoing small strains. Arch Appl Mech 72:300–317. doi:10.1007/s00419-002-0212-2

Munier P, Gordeyeva K, Bergström L, Fall AB (2016) Directional freezing of nanocellulose dispersions aligns the rod-like particles and produces low-density and robust particle networks. Biomacromolecules. doi:10.1021/acs.biomac.6b00304

Natesaiyer K, Chan C, Sinha-Ray S et al (2015) X-ray CT imaging and finite element computations of the elastic properties of a rigid organic foam compared to experimental measurements: insights into foam variability. J Mater Sci 50:4012–4024. doi:10.1007/s10853-015-8958-4

Pääkkö M, Ankerfors M, Kosonen H et al (2007) Enzymatic hydrolysis combined with mechanical shearing and high-pressure homogenization for nanoscale cellulose fibrils and strong gels. Biomacromolecules 8:1934–1941

Pääkkö M, Vapaavuori J, Silvennoinen R et al (2008) Long and entangled native cellulose I nanofibers allow flexible aerogels and hierarchically porous templates for functionalities. Soft Matter 4:2492. doi:10.1039/b810371b

Sehaqui H, Salajková M, Zhou Q, Berglund LA (2010) Mechanical performance tailoring of tough ultra-high porosity foams prepared from cellulose I nanofiber suspensions. Soft Matter 6:1824. doi:10.1039/b927505c

Sehaqui H, Zhou Q, Ikkala O, Berglund LA (2011) Strong and tough cellulose nanopaper with high specific surface area and porosity. Biomacromolecules 12:3638–3644. doi:10.1021/bm2008907

Srinivasa P, Kulachenko A, Aulin C (2015) Experimental characterisation of nanofibrillated cellulose foams. Cellulose 22:3739–3753. doi:10.1007/s10570-015-0753-5

Svagan AJ, Samir MASA, Berglund LA (2008) Biomimetic foams of high mechanical performance based on nanostructured cell walls reinforced by native cellulose nanofibrils. Adv Mater 20:1263–1269. doi:10.1002/adma.200701215

Tchang Cervin N, Aulin C, Larsson PT, Wågberg L (2012) Ultra porous nanocellulose aerogels as separation medium for mixtures of oil/water liquids. Cellulose 19:401–410. doi:10.1007/s10570-011-9629-5

Wågberg L, Decher G, Norgren M et al (2008) The build-up of polyelectrolyte multilayers of microfibrillated cellulose and cationic polyelectrolytes. Langmuir 24:784–795